Supplemental Information for Spintwistronics: Photonic Bilayer Topological Lattices Tuning Extreme Spin-Orbit Interactions

Peng Shi[1,†,*], Xinxin Gou[1,†], Qiang Zhang[1,†,*], Weiyu Wei[1], Haijun Wu[2,3,4], Songze Li[1],
Zhihan Zhu[4], Yijie Shen[2,3*] and Xiaocong Yuan[1,5,*]

[1]*Nanophotonics Research Center, Shenzhen Key Laboratory of Micro-Scale Optical Information Technology & Institute of Microscale Optoelectronics, Shenzhen University, Shenzhen 518060, China*
[2]*Division of Physics and Applied Physics, School of Physical and Mathematical Sciences, Nanyang Technological University, Singapore 637378, Singapore*
[3]*Centre for Disruptive Photonic Technologies, The Photonics Institute, Nanyang Technological University, Singapore 637378, Singapore*
[4]*Wang Da-Heng Center, HLJ Key Laboratory of Quantum Control, Harbin University of Science and Technology, Harbin, 150080 China*
[5]*Zhejiang Lab, Research Center for Humanoid Sensing, Research Institute of Intelligent Sensing, Hangzhou 311100, China*

[†]There authors contribute equally to the work
[*]Authors to whom correspondence should be addressed: pittshiustc@gmail.com, zhangqiang@szu.edu.cn, yijie.shen@ntu.edu.sg, xcyuan@szu.edu.cn,

Contents:

I. Photonic topological spin sublattices for Moiré superlattices

In our work, we investigate the photonic topological Moiré spin lattices formed at the metal/air interface, where the transverse magnetic (TM) surface plasmon polaritons (SPP) modes [S1] can be effectively excited using a high-numerical-aperture (NA=1.49) oil immersion lens in conjunction with a radially polarized monochromatic (angular frequency is given by ω), time-harmonic (time-dependent is given by $\exp[-i\omega t]$) electromagnetic (EM) field carrying orbital angular momentum (OAM) defined by quantum number l. By customizing the rotational symmetry, we create various photonic topological sublattices that *strictly adhere to translational and rotational symmetries*, with threefold (C_3), fourfold (C_4) and sixfold (C_6) rotational configurations [S2], respectively. The electric field component (E_z) in the direction normal to the interface within the air half-space is described by the Hertz potential Ψ [S3]

$$E_z = \Psi = A\sum_{n=1}^{N} e^{il\theta_n} e^{i\beta \mathbf{r}_\perp \cdot \mathbf{e}_n} e^{-k_z z} , \tag{S1}$$

where $\theta_n = 2n\pi/N$, $\mathbf{e}_n = (\cos\theta_n, \sin\theta_n)$ with $n = 1, \ldots, N$ and N representing the N-fold rotational symmetry. Here, β and ik_z represent the wavenumbers in the horizontal (propagation constant) and vertical (evanescent wavenumber) directions, respectively. They satisfy the relation $\beta^2 - k_z^2 = k^2$, where k is the wavenumber in the air half-space. The horizontal position vector is $\mathbf{r}_\perp = (x, y) = \rho(\cos\varphi, \sin\varphi)$, with ρ and φ denoting the radial and azimuthal coordinates in cylindrical coordinates. Here, i denotes the imaginary unit. The spin angular momenta (SAMs) $\mathbf{S}$ of these fields can be given by the spin-momentum relations [S4]

$$\mathbf{S} = \frac{\varepsilon\beta^2}{4\omega}\mathrm{Im}\left(\nabla\Psi^* \times \nabla\Psi\right) = -\frac{\varepsilon\beta^2}{4\omega}\left\langle \nabla\Psi \middle| \times i \middle| \nabla\Psi \right\rangle . \tag{S2}$$

The topological skyrmion number of these topological spin lattices, as defined in [S5], is given by

$$n_{sk} = \frac{1}{4\pi}\iint_{cell} \mathbf{m} \cdot \left(\frac{\partial \mathbf{m}}{\partial x} \times \frac{\partial \mathbf{m}}{\partial y}\right) d^2\mathbf{r} , \tag{S3}$$

which quantifies how many times the normalized spin vector $\mathbf{m}(\mathbf{r}) = \mathbf{m}(x, y) = \mathbf{S}(x, y)/|\mathbf{S}(x, y)|$ wraps the unit sphere. Specifically, from Eq. (S1), the electric field component E_z exhibits periodicity concerning the quantum number of total angular momentum (TAM), meaning that the SAM distributions also show similar periodicity with respect to TAM (i.e., the quantum number l of OAM). To visually demonstrate this periodicity, we present the SAM distributions and topological textures for N = 3, 4 and 6 in **FIG. S1** to **FIG. S3**, respectively. These topological textures are regarded as sublattices for constructing photonic Moiré superlattices.

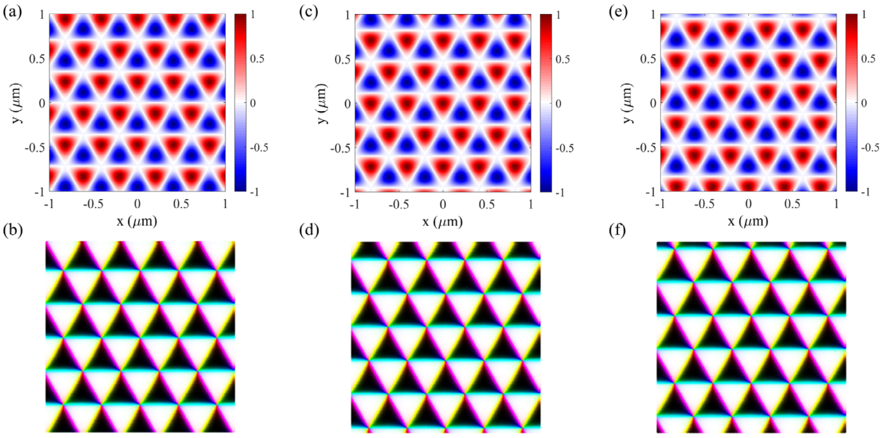

FIG. S1. The SAM component in the normal direction (S_z) and the topological spin textures within the air half-space exhibit C_3 rotational symmetry. Panels (a), (c), and (e) show the distributions of S_z, while panels (b), (d), and (f) display the corresponding topological spin textures for TAM quantum number l = 0, 1, and 2, respectively. Under C_3 symmetry, the periodicity relative to the TAM quantum number is 3 in. In (b), (d), and (f), white and black colors denote 'up' and 'down' spin states, while other colors represent inclined or twisted spin states. These topological spin lattices can be interpreted as combinations of meron sublattices, each with a skyrmion number $n_{sk} = \pm 1/2$.

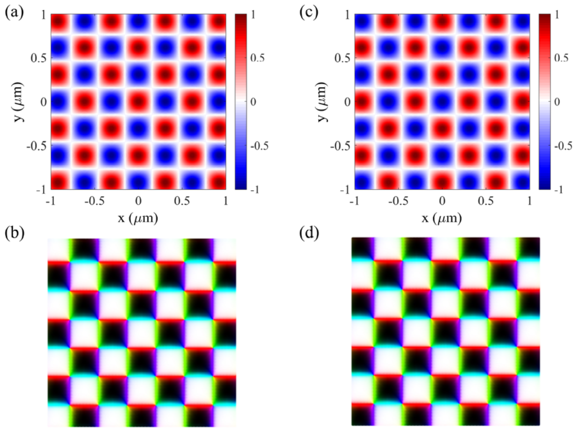

FIG. S2. The S_z component and topological spin textures within the air half-space exhibit C_4 rotational symmetry. Panels (a) and (c) show the distributions of S_z, while panels (b) and (d) display the topological spin textures for TAM quantum number $l = 1$ and 3, respectively. Under C_4 symmetry, the periodicity in relation to the TAM quantum number is 4. Notably, the SAM vanishes when $l = 0$ and 2, resulting in the excitation of stationary waves. The topological spin textures in (b) and (d) can be interpreted as combinations of meron sublattices, each with a skyrmion number $n_{sk} = \pm 1/2$.

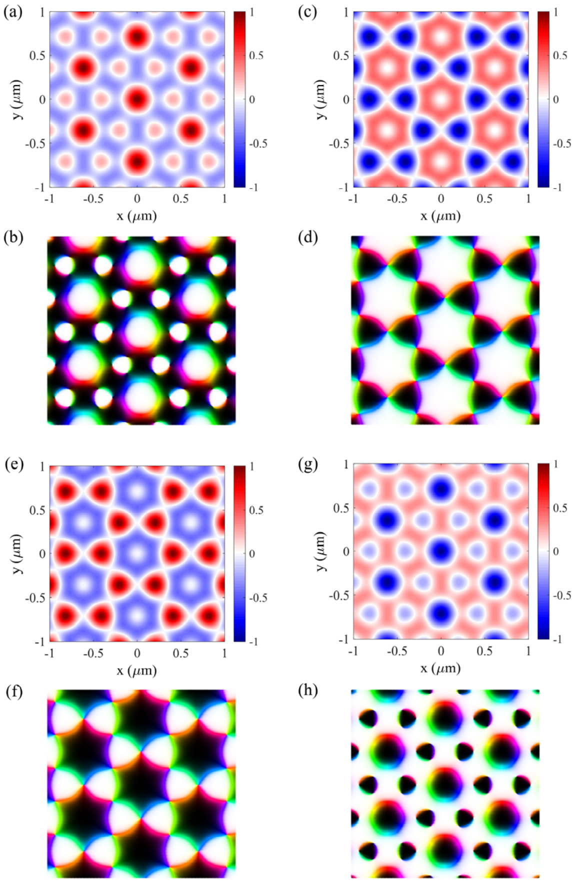

FIG. S3. The S_z component and topological spin textures within the air half-space exhibit C_6 rotational symmetry. Panels (a), (c), (e), and (g) show the distributions of S_z, while panels (b), (d), (f), and (h) present the topological spin textures for TAM quantum numbers $l = 1$, 2, 4, and 5, respectively. In C_6 symmetry, the periodicity relative to the TAM quantum number is 6. Examining the spin textures, we observe that no region has an integer-integrated skyrmion number density. We thus refer to these structures as "fractal skyrmion lattices", as the spin lattices in (b), (d), (f), and (h) can be interpreted as combinations of two fractal skyrmion sublattices with a skyrmion number $n_{sk} = \pm 1$ [S2]. Note that S_z vanishes for $l = 0$ and 3, and no topological spin textures exist in these cases.

II. Formation of photonic Moiré spin superlattices

To create the Moiré lattice, we superimpose **a pair of** topological sublattices by rotating them clockwise and counter-clockwise about the *z*-axis by angles $\pm\vartheta$ (resulting in an intersection angle of 2ϑ). The inclined topological lattice is then obtained using the rotation matrix $\hat{R}_z(+\vartheta)$

$$\mathbf{r}_\perp(+\vartheta) = \hat{R}_z(+\vartheta)\mathbf{r}_\perp = \begin{pmatrix} \cos\vartheta & -\sin\vartheta \\ \sin\vartheta & \cos\vartheta \end{pmatrix}\begin{pmatrix} \rho\cos\varphi \\ \rho\sin\varphi \end{pmatrix} = \rho\begin{pmatrix} \cos(\varphi+\vartheta) \\ \sin(\varphi+\vartheta) \end{pmatrix} \tag{S4}$$

The inclined electric field component in the normal direction (E_z) of each sublattice within the air half-space is be given by

$$E_z(+\vartheta) = A\sum_{n=1}^{N} e^{il(\theta_n+\vartheta)} e^{i\beta\mathbf{r}_\perp(\vartheta)\cdot\mathbf{e}_n} e^{-k_z z}\ . \tag{S5}$$

The superposed E_z field can be expressed as

$$E_z = E_z(+\vartheta) + E_z(-\vartheta)\,. \tag{S6}$$

To illustrate the conditions for forming the Moiré lattice under C_4 rotational symmetry, as depicted in **FIG.** S4(a), the expression for E_z can be given by

$$E_z = 2Ae^{-k_z z}\begin{bmatrix} +\cos\left[\beta(x\sin\vartheta + y\cos\vartheta) - l\dfrac{\pi}{2}\right]e^{-i[l\vartheta - l\pi]} + \cos\left[\beta(x\sin\vartheta - y\cos\vartheta) + l\dfrac{\pi}{2}\right]e^{+i[l\vartheta + l\pi]} \\ +\cos\left[\beta(x\cos\vartheta + y\sin\vartheta) + l\dfrac{\pi}{2}\right]e^{+i\left[l\vartheta + l3\frac{\pi}{2}\right]} + \cos\left[\beta(x\cos\vartheta - y\sin\vartheta) + l\dfrac{\pi}{2}\right]e^{-i\left[l\vartheta - l3\frac{\pi}{2}\right]} \end{bmatrix}. \tag{S7}$$

The S_z component and spin texture of the Moiré lattice formed by the C_4 rotational symmetric sublattices with l =1 and intersection angles 2ϑ = arctan(5/12) and arctan(3/4) are presented in **FIG.** S4(b-c) and **FIG.** S4(d-e), respectively.

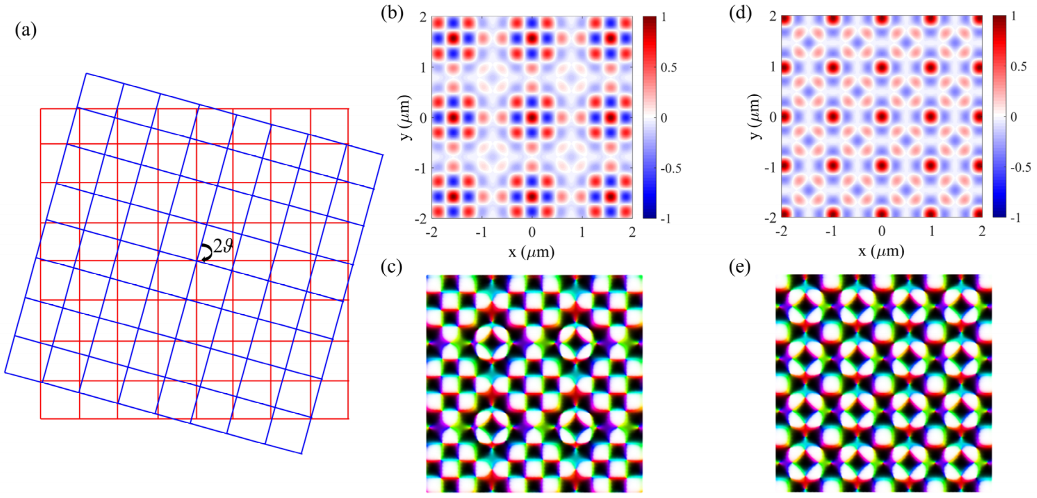

FIG. S4. (a) Moiré superlattices generated by the superimposed C_4 rotational symmetric sublattices, with axes mutually rotated by the angle 2ϑ. (b) The S_z component and (c) the topological spin texture of the Moiré lattice for l =1 with an intersection Moiré angle 2ϑ = arctan(5/12); (d) The S_z component and (e) the topological spin texture of the Moiré lattice for l =1 with an intersection Moiré angle 2ϑ = arctan(3/4). In these instances, the Moiré superlattices exhibit clear translational and rotational symmetries.

In addition, to determine which angles can form the Moiré lattices, we analyze the real part of E_z. After some straightforward derivations, we find that when the TAM quantum number is odd ($l = 2n + 1$), the real part can be re-expressed as

$$\mathrm{Re}\{E_z\} = 4Ae^{-k_z z}\begin{bmatrix} -\cos[\beta x\sin\vartheta]\sin[\beta y\cos\vartheta - n\pi]\cos[l\vartheta] \\ -\cos[\beta x\cos\vartheta + n\pi]\sin[\beta y\sin\vartheta]\sin[l\vartheta]\sin\left[(n+1)\pi + \dfrac{\pi}{2}\right] \end{bmatrix}. \tag{S8}$$

It is important to note that cos($l\vartheta$) and sin($l\vartheta$) are not always zero when $l \neq 0$. Therefore, we conclude that the Moiré superlattice exhibits periodicity when

$$\begin{cases} \beta y\cos\vartheta - n\pi = n_1\pi \\ \beta y\sin\vartheta = n_2\pi \end{cases} \Rightarrow \tan\vartheta = \frac{n_2}{n+n_1}. \tag{S9}$$

Here, n_1 and n_2 can be any integers. Conversely, when the TAM quantum number is even ($l = 2n$), the real part can be re-expressed as

$$\mathrm{Re}\{E_z\} = 4Ae^{-k_z z}\begin{bmatrix} +\cos[\beta x\sin\vartheta]\cos[\beta y\cos\vartheta - n\pi]\cos[l\vartheta] \\ +\cos[\beta x\cos\vartheta + n\pi]\cos[\beta y\sin\vartheta]\cos[l\vartheta]\cos[n\pi] \end{bmatrix}. \tag{S10}$$

We obtain that the Moiré superlattice is periodic when

$$\begin{cases} \beta y\cos\vartheta - n\pi = (2n_3+1)\dfrac{\pi}{2} \\ \beta y\sin\vartheta = (2n_4+1)\dfrac{\pi}{2} \end{cases} \Rightarrow \tan\vartheta = \frac{2n_4+1}{2n_3+2n+1}. \tag{S11}$$

By comparing Eq. (S9) with Eq. (S11), we find that the restrictions on the even quantum numbers are more stringent than those on the odd quantum numbers. Therefore, using Eq. (S11), we can derive the Moiré angle as

$$2\vartheta = \arctan\frac{(2n_4+1)(2n+2n_3+1)}{2(n+n_3+n_4+1)(n+n_3-n_4)}. \tag{S12}$$

This indicates that *the denominator must be even while the numerator should be odd.* For example, with $n_4 = 0$ and $n + n_3 = 2$, we obtain $2\vartheta = \arctan(5/12)$. Similarly, with $n_4 = 0$ and $n + n_3 = 1$, we obtain $2\vartheta = \arctan(3/4)$. Given that n, n_3 and n_4 can be any integers, we define $m_1 = n + n_3$ and $m_2 = n_4$. Consequently, the Moiré angle must satisfy the relation

$$2\vartheta_{C4} = \arctan\frac{(2m_2+1)(2m_1+1)}{2(m_1+m_2+1)(m_1-m_2)}. \tag{S13}$$

Subsequently, to explore the conditions for forming the Moiré lattice under C_6 rotational symmetry, as illustrated in **FIG.** S5(a), the expression for E_z can be given by

$$E_z = 2Ae^{-k_z z}\begin{bmatrix} +\cos\left[\beta x\left(\dfrac{\sqrt{3}}{2}\sin\vartheta - \dfrac{1}{2}\cos\vartheta\right) - l\vartheta + l\dfrac{\pi}{6}\right]e^{+i\left[\beta\left(\frac{1}{2}y\sin\vartheta + \frac{\sqrt{3}}{2}y\cos\vartheta\right) + l\frac{\pi}{2}\right]} \\ +\cos\left[\beta x\left(\dfrac{\sqrt{3}}{2}\sin\vartheta + \dfrac{1}{2}\cos\vartheta\right) - l\vartheta - l\dfrac{\pi}{6}\right]e^{-i\left[\beta\left(\frac{1}{2}y\sin\vartheta - \frac{\sqrt{3}}{2}y\cos\vartheta\right) - l\frac{\pi}{2}\right]} \\ +\cos\left[\beta x\left(\dfrac{\sqrt{3}}{2}\sin\vartheta + \dfrac{1}{2}\cos\vartheta\right) + l\vartheta + l\dfrac{\pi}{6}\right]e^{+i\left[\beta\left(\frac{1}{2}y\sin\vartheta - \frac{\sqrt{3}}{2}y\cos\vartheta\right) + l\frac{3\pi}{2}\right]} \\ +\cos\left[\beta x\left(\dfrac{\sqrt{3}}{2}\sin\vartheta - \dfrac{1}{2}\cos\vartheta\right) + l\vartheta - l\dfrac{\pi}{6}\right]e^{-i\left[\beta\left(\frac{1}{2}y\sin\vartheta + \frac{\sqrt{3}}{2}y\cos\vartheta\right) - l\frac{3\pi}{2}\right]} \\ +\cos\left[\beta(x\cos\vartheta + y\sin\vartheta) + l\dfrac{\pi}{2}\right]e^{+i\left[l\vartheta + l\frac{3\pi}{2}\right]} + \cos\left[\beta(x\cos\vartheta - y\sin\vartheta) + l\dfrac{\pi}{2}\right]e^{-i\left[l\vartheta - l\frac{3\pi}{2}\right]} \end{bmatrix}. \tag{S14}$$

The S_z component and spin texture of the Moiré lattice formed by the C_6 rotational symmetric sublattices when $l=1$ and Moiré angle $2\vartheta = \arctan(11/14)$ and $\arctan(13/19)$ are shown in **FIG.** S5(b-c) and **FIG.** S5(d-e), respectively.

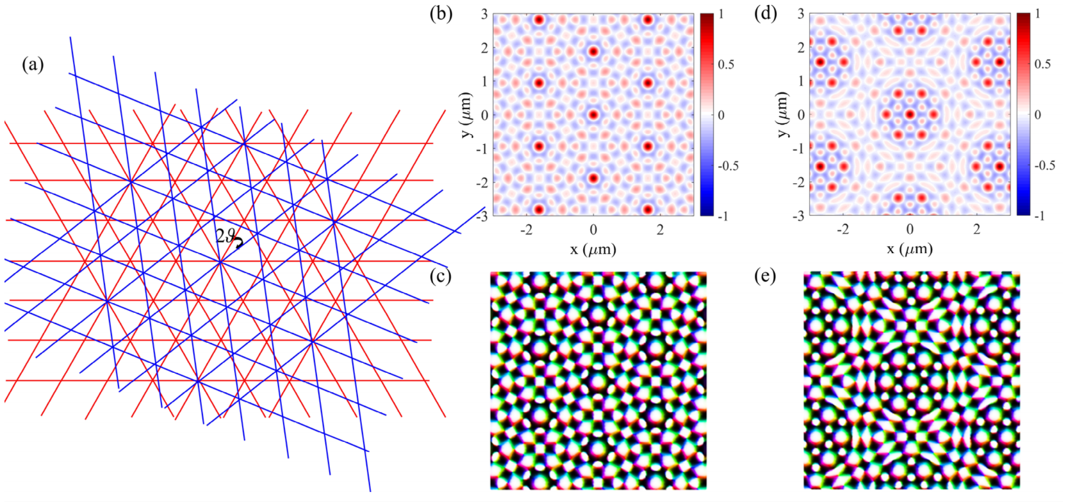

FIG. S5. (a) Moiré lattices generated by the C_6 rotational symmetric sublattices, with axes mutually rotated by the angle 2ϑ. (b) The S_z component and (c) the topological spin texture of the Moiré lattice formed by the C_6 rotational symmetric sublattice when $l=1$ and the intersection Moiré angle $2\vartheta = \arccos(11/14)$. (d) The S_z component and (e) the topological spin texture of the Moiré lattice formed by the C_6 rotational symmetric sublattice when $l=1$ and the intersection angle $2\vartheta = \arccos(13/19)$. In these instances, the Moiré superlattices exhibit clear translational and rotational symmetries.

Here, we also consider the real part of E_z

$$\mathrm{Re}\{E_z\} = 2Ae^{-k_z z}\,\mathrm{Re}\left[\begin{array}{l} +\cos\left[+\beta x\left(\frac{\sqrt{3}}{2}\sin\vartheta-\frac{1}{2}\cos\vartheta\right)-l\vartheta+l\frac{\pi}{6}\right]\cos\left[+\beta y\left(\frac{1}{2}\sin\vartheta+\frac{\sqrt{3}}{2}\cos\vartheta\right)+l\frac{\pi}{2}\right] \\ +\cos\left[+\beta x\left(\frac{\sqrt{3}}{2}\sin\vartheta+\frac{1}{2}\cos\vartheta\right)-l\vartheta-l\frac{\pi}{6}\right]\cos\left[+\beta y\left(\frac{1}{2}\sin\vartheta-\frac{\sqrt{3}}{2}\cos\vartheta\right)-l\frac{\pi}{2}\right] \\ +\cos\left[+\beta x\left(\frac{\sqrt{3}}{2}\sin\vartheta+\frac{1}{2}\cos\vartheta\right)+l\vartheta+l\frac{\pi}{6}\right]\cos\left[+\beta y\left(\frac{1}{2}\sin\vartheta-\frac{\sqrt{3}}{2}\cos\vartheta\right)+l\frac{3\pi}{2}\right] \\ +\cos\left[+\beta x\left(\frac{\sqrt{3}}{2}\sin\vartheta-\frac{1}{2}\cos\vartheta\right)+l\vartheta-l\frac{\pi}{6}\right]\cos\left[+\beta y\left(\frac{1}{2}\sin\vartheta+\frac{\sqrt{3}}{2}\cos\vartheta\right)-l\frac{3\pi}{2}\right] \\ +2\cos\left[+\beta x\cos\vartheta+l\frac{\pi}{2}\right]\cos\left[+\beta y\sin\vartheta\right]\cos\left[l\vartheta\right]\cos\left[l\frac{3\pi}{2}\right] \\ -2\sin\left[+\beta x\cos\vartheta+l\frac{\pi}{2}\right]\sin\left[+\beta y\sin\vartheta\right]\sin\left[l\vartheta\right]\sin\left[l\frac{3\pi}{2}\right] \end{array}\right]. \tag{S15}$$

It can be observed that the terms $\cos[l3\pi/2]$ and $\sin[l3\pi/2]$ do not vanish simultaneously. Therefore, when the TAM quantum number is an odd number ($l = 2n + 1$), the superposed Moiré lattice is periodic when

$$\tan\vartheta = \sqrt{3}\frac{n_1+n_2+1}{n_1-n_2-2n-1}. \tag{S16}$$

Here, n_1 and n_2 can be any integers. Conversely, when the TAM quantum number is an even number ($l = 2n$), the superposed Moiré lattice is periodic when

$$\tan\vartheta = \sqrt{3}\frac{n_3+n_4}{n_3-n_4-2n}. \tag{S17}$$

Here, n_3 and n_4 can be any integers. Since both restrictions coincide, we can summarize them into a single restriction. Therefore, the intersection angle between the two topological spin sublattice can be expressed as

$$2\theta = \arccos\left[\frac{\left(n_3-n_4-2n\right)^2-3\left(n_3+n_4\right)^2}{\left(n_3-n_4-2n\right)^2+3\left(n_3+n_4\right)^2}\right]. \tag{S18}$$

For example, with $n_3 = 1$, $n_4 = 0$ and $n = -2$, we obtain $2\vartheta = \arccos(11/14)$. Similarly, with $n_3 = 2$, $n_4 = 0$, and $n = -3$, we obtain $2\vartheta = \arccos(13/19)$. Since n, n_3, and n_4 can be any integers, we define $m_1 = n_3 - n$ and $m_2 = n_4 + n$. Consequently, the Moiré angle must satisfy the relation

$$2\theta_{\mathrm{C}6} = \arccos\left[\frac{\left(m_1-m_2\right)^2-3\left(m_1+m_2\right)^2}{\left(m_1-m_2\right)^2+3\left(m_1+m_2\right)^2}\right]. \tag{S19}$$

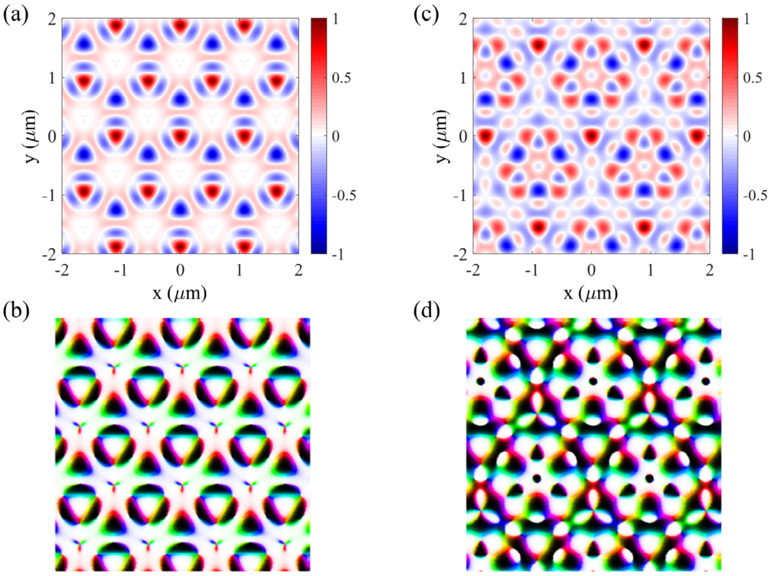

FIG. S6. (a) Moiré lattices generated by the C_3 rotational symmetric sublattices, with axes mutually rotated by the angle 2ϑ. (b) The S_z component and (c) the topological spin texture of the Moiré lattice formed by the C_3 rotational symmetric sublattice when $l = 1$ and the Moiré angle $2\vartheta = \arccos(11/14)$. (d) The S_z component and (e) the topological spin texture of the Moiré lattice formed by the C_3 rotational symmetric sublattice when $l = 1$ and the moiré angle $2\vartheta = \arccos(13/19)$.

Finally, for the Moiré lattice constructed from the sublattice in C_3 rotational symmetry, the expression for E_z can be given by

$$E_z = Ae^{-k_z z}e^{il\vartheta}\begin{bmatrix} 1+2\cos\left[+\frac{\sqrt{3}}{2}k_{sp}\left[x\sin[\vartheta]-y\cos[\vartheta]\right]-l\frac{2\pi}{3}\right] \\ \exp\left[-\frac{3}{2}ik_{sp}\left[x\cos[\vartheta]+y\sin[\vartheta]\right]\right] \end{bmatrix}\exp\left[+ik_{sp}x\cos[\vartheta]+ik_{sp}y\sin[\vartheta]\right]. \tag{S20}$$

Here, we also consider the real part of E_z as

$$\mathrm{Re}\{E_z\} = Ae^{-k_z z}\begin{bmatrix} +2\cos\left[+\frac{\sqrt{3}}{2}\beta x\sin[\vartheta]-\frac{\sqrt{3}}{2}\beta y\cos[\vartheta]-l\frac{2\pi}{3}\right]\cos\left[-\frac{1}{2}\beta x\cos[\vartheta]-\frac{1}{2}\beta y\sin[\vartheta]+l\vartheta\right] \\ +\cos\left[+\beta x\cos[\vartheta]+\beta y\sin[\vartheta]+l\vartheta\right] \end{bmatrix}. \tag{S21}$$

From the equation, we find that the superposed lattice is periodic when

$$\tan\vartheta = \frac{\sqrt{3}n_3}{n_2-n_1}. \tag{S22}$$

Thus, the intersection angle between the two topological spin sublattice can be expressed as

$$2\vartheta = \arccos\frac{\left(n_2 - n_1\right)^2 - 3n_3^2}{\left(n_2 - n_1\right)^2 + 3n_3^2}. \tag{S23}$$

Here, n_1, n_2 and n_3 can be any integers. For example, with $n_1 - n_2 = 5$ and $n_3 = 1$, we obtain $2\vartheta = \arccos(11/14)$. Similarly, with $n_1 - n_2 = 4$ and $n_3 = 1$, we obtain $2\vartheta = \arccos(13/19)$. Since n_1, n_2, and n_3 can be any integers, we define $m_1 = n_2 - n_1$ and $m_2 = n_3$. Consequently, the Moiré angle must satisfy the relation

$$2\vartheta_{\mathrm{C}3} = \arccos\frac{m_1^2 - 3m_2^2}{m_1^2 + 3m_2^2}. \tag{S24}$$

Notably, the condition given by Eq. (S24) is consistent with that provided by Eq. (S19). The S_z component and spin texture of the Moiré lattice formed by the C_3 rotational symmetric sublattices, when $l = 1$ and the intersection angles are $2\vartheta = \arctan(11/14)$ and $\arctan(13/19)$, can be seen in **FIG.** S6(a-b) and **FIG.** S6(c-d), respectively.

III. Periodicity of photonic Moiré superlattices with respect to quantum number of total angular momentum

In contrast to the photonic Moiré lattices formed by the electric field [S6], the photonic Moiré topological spin lattices are significantly influenced by the quantum number l of the TAM. It is evident that the photonic Moiré topological spin lattices vary periodically with respect to l.

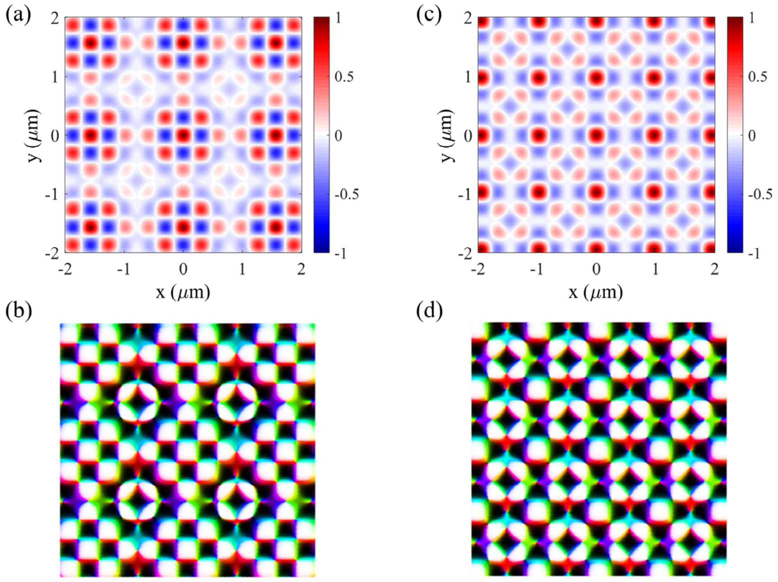

FIG. S7. The periodicity of the quantum number l of the TAM in Moiré lattices generated by the superimposed C_4 rotational symmetric sublattices, with axes mutually rotated by the angle 2ϑ, is illustrated as follows. (a) The S_z component and (b) the topological spin texture of the Moiré lattice when $l = 17$ and the intersection angle $2\vartheta = \arctan(5/12)$. Notably, the distributions of S_z and the topological spin texture are identical to those for $l = 1$ shown in **FIG.** S4(b-c). (c) The S_z component and (d) the topological spin texture of the Moiré lattice when $l = 157$ and the intersection angle $2\vartheta = \arctan(3/4)$. Similarly, it can be observed that the distributions of S_z and the topological spin texture match those for $l = 1$ in **FIG.** S4(d-e).

We will first consider the photonic Moiré lattices in C_4 rotational symmetry as an example. From Eq. (S7), the difference between two photonic Moiré lattices with different quantum numbers l_1 and l_2 can be expressed as

$$\begin{aligned} & E_{z,l_2} - E_{z,l_1} \\ & = 4Ae^{-k_z z} \sin\frac{(l_1 - l_2)\vartheta}{2} \begin{bmatrix} -\sin\left[\beta x \sin\vartheta - \frac{l_1 + l_2}{2}\vartheta\right] e^{+il_1\frac{\pi}{2}} e^{+i\beta y\cos\vartheta} + \sin\left[\beta x \sin\vartheta + \frac{l_1 + l_2}{2}\vartheta\right] e^{-il_1\frac{\pi}{2}} e^{-i\beta y\cos\vartheta} \\ -\sin\left[\beta y \sin\vartheta - \frac{l_1 + l_2}{2}\vartheta\right] e^{il_1\pi} e^{-i\beta x\cos\vartheta} + \sin\left[\beta y \sin\vartheta + \frac{l_1 + l_2}{2}\vartheta\right] e^{il_1 2\pi} e^{+i\beta x\cos\vartheta} \end{bmatrix}. \end{aligned} \tag{S25}$$

Obviously, the terms in the square brackets are not always zero. Thus, the periodicity of photonic Moiré lattices depends on the condition $\sin(l_1 - l_2)\vartheta/2 = 0$, which holds when $(l_1 - l_2) \bmod 4 = 0$. In summary, the period p is given by $p = l_1 - l_2 = n\pi/\vartheta$ with the additional condition that $p \bmod 4 = 0$. *It is worth noting that, in general, the quantity $n\pi/\vartheta$ is not strictly an integer*. However, if $p = n\pi/\vartheta$ can be approximated as an integer, it can represent the period of the photonic Moiré lattices concerning the quantum number l of the TAM. For example, for the photonic Moiré lattices formed by the C_4 rotational symmetric sublattice with an intersection Moiré angle $2\vartheta = \arctan(5/12)$, we find $p = n\pi/\vartheta \approx 15.915 \approx 16$ when $n = 1$, which clearly satisfies $16 \bmod 4 = 0$. Thus, $p = 16$ can be considered the period of these photonic Moiré lattices, as shown in **FIG.** S4(b-c) and **FIG.** S7(a-b). Conversely, for the photonic Moiré lattices formed by the C_4 rotational symmetric sublattices with the intersection Moiré angle $2\vartheta = \arctan(3/4)$, to satisfy both conditions, we find that $n = 16$ and $p = 156$ can be regarded as the period of these photonic Moiré lattices, which can be seen in **FIG.** S4(d-e) and **FIG.** S7(c-d).

Similarly, for the photonic Moiré lattices in C_6 rotational symmetry, the difference between two photonic Moiré lattices characterized by different quantum numbers l_1 and l_2 can be expressed by

$$
\begin{aligned}
&E_{z,l_2}-E_{z,l_1}\\
&=4Ae^{-k_z z}\sin\frac{(l_1-l_2)\vartheta}{2}\left[\begin{array}{l}
-e^{il_1\frac{\pi}{3}}e^{i\beta\left[+\frac{1}{2}x\cos\vartheta+\frac{\sqrt{3}}{2}y\cos\vartheta\right]}\sin\left[+\frac{\sqrt{3}}{2}\beta x\sin\vartheta-\frac{1}{2}\beta y\sin\vartheta-\frac{l_1+l_2}{2}\vartheta\right]\\
+e^{il_1\frac{4\pi}{3}}e^{i\beta\left[-\frac{1}{2}x\cos\vartheta-\frac{\sqrt{3}}{2}y\cos\vartheta\right]}\sin\left[+\frac{\sqrt{3}}{2}\beta x\sin\vartheta-\frac{1}{2}\beta y\sin\vartheta+\frac{l_1+l_2}{2}\vartheta\right]\\
-e^{il_1\frac{2\pi}{3}}e^{i\beta\left[-\frac{1}{2}x\cos\vartheta+\frac{\sqrt{3}}{2}y\cos\vartheta\right]}\sin\left[+\frac{\sqrt{3}}{2}\beta x\sin\vartheta+\frac{1}{2}\beta y\sin\vartheta-\frac{l_1+l_2}{2}\vartheta\right]\\
+e^{il_1\frac{5\pi}{3}}e^{i\beta\left[+\frac{1}{2}x\cos\vartheta-\frac{\sqrt{3}}{2}y\cos\vartheta\right]}\sin\left[+\frac{\sqrt{3}}{2}\beta x\sin\vartheta+\frac{1}{2}\beta y\sin\vartheta+\frac{l_1+l_2}{2}\vartheta\right]\\
-e^{il_1\pi}e^{-i\beta x\cos\vartheta}\sin\left[\beta y\sin\vartheta-\frac{l_1+l_2}{2}\vartheta\right]+e^{il_2 2\pi}e^{+i\beta x\cos\vartheta}\sin\left[\beta y\sin\vartheta+\frac{l_1+l_2}{2}\vartheta\right]
\end{array}\right].
\end{aligned}
\tag{S26}
$$

The periodicity of photonic Moiré lattices in C_6 rotational symmetry depends on the condition $\sin(l_1 - l_2)\vartheta/2 = 0$, which holds when $(l_1 - l_2) \bmod 6 = 0$. This leads to the period being expressed as $p = l_1 - l_2 = n\pi/\vartheta$, with the requirement that $p \bmod 6 = 0$. For example, for the photonic Moiré lattices formed by the sublattice with an intersection angle $2\vartheta = \arccos(11/14)$, we find $p = n\pi/\vartheta \approx 65.946 \approx 66$ when $n = 7$, which satisfies $66 \bmod 6 = 0$. Thus, $p = 66$ can be regarded as the period of these photonic Moiré lattices, as shown in **FIG. S**5(b-c) and **FIG. S**8(a-b). In contrast, for the photonic Moiré lattices formed by the C_6 rotational symmetric sublattice with the Moiré angle $2\vartheta = \arccos(13/19)$, to meet both conditions, we find that $n = 32$ and $p = 246$ can be considered the period of these photonic Moiré lattices, which can be seen in **FIG. S**5(d-e) and **FIG. S**8(c-d).

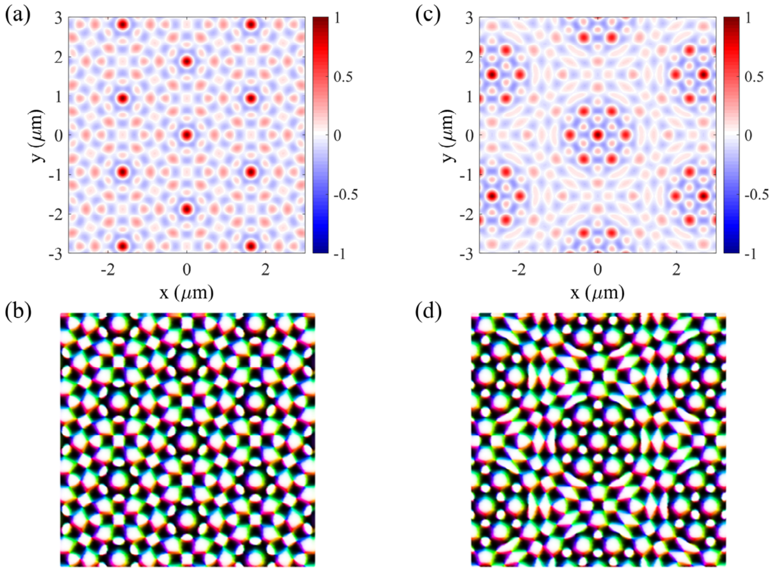

FIG. S8. The periodicity with respect to the quantum number l of TAM in Moiré lattices generated by C_4 rotational symmetric sublattices, where the axes are mutually rotated by the angle 2ϑ, can be observed as follows: (a) The distribution of S_z and (b) the topological spin texture of the Moiré lattice formed by the C_4 rotational symmetric sublattice when $l = 67$ and the intersection angle $2\vartheta = \arccos(11/14)$.exhibit the same patterns as those for $l = 1$ shown in **FIG. S**5(b-c). Similarly, (c) the distribution of S_z and (d) the topological spin texture of the Moiré lattice formed by the C_3 rotational symmetric sublattice when $l = 247$ and the intersection angle $2\vartheta = \arccos(13/19)$ also match the distributions for $l = 1$ as depicted in **FIG. S**5(d-e).

Similarly, for the photonic Moiré lattices in C_3 rotational symmetry, the difference between two photonic Moiré lattices characterized by different quantum numbers l_1 and l_2 can be expressed by

$$\begin{aligned}
&E_{z,l_2} - E_{z,l_1} \\
&= 2iAe^{-k_z z}\sin\left[\frac{l_2-l_1}{2}\vartheta\right]\exp\left[+i\frac{l_2+l_1}{2}\vartheta\right]\left[\begin{array}{l} +2\cos\left[\begin{array}{l} +\frac{\sqrt{3}}{2}\beta x\sin[\vartheta] \\ -\frac{\sqrt{3}}{2}\beta y\cos[\vartheta]-l\frac{2\pi}{3} \end{array}\right]\exp\left[\begin{array}{l} -\frac{i}{2}\beta x\cos[\vartheta] \\ -\frac{i}{2}\beta y\sin[\vartheta] \end{array}\right] \\ +\exp\left[+i\beta x\cos[\vartheta]+i\beta y\sin[\vartheta]\right] \end{array}\right].
\end{aligned} \tag{S27}$$

By comparing Eq. (S26) with Eq. (S27), we observe a similar periodicity in the Moiré lattices constructed by the C_3 rotational symmetric sublattices and those formed by the C_6 rotational symmetric sublattices.

IV. Novel topological and extreme spin-orbit coupling properties of photonic Moiré spin superlattices

As mentioned earlier, the photonic Moiré topological spin lattices can be constructed by the superposition of two sublattices with an intersection Moiré angle 2ϑ. In addition to the periodicity with respect to the quantum number l of TAM analyzed above, there are several novel topological spin lattices and phenomena that emerge within the Moiré spin lattices.

Real Skyrmion lattices formed by meron sublattices

Previously, only the meron lattices with a topological skyrmion number $n_{sk} = \pm 1/2$ could be formed in systems with C_3 and C_4 rotational symmetries [S2, S3], as shown in **FIG. S**1 and **FIG. S**2. In contrast, only fractal skyrmion lattices with a topological skyrmion number $n_{sk} = \pm 1$ were formed in systems with C_6 rotational symmetries [S2]. However, photonic Moiré lattices offer an increased degree of freedom through the Moiré angle, enabling the construction of novel photonic topological textures and new topologies within certain rotationally symmetric systems. For instance, the Moiré lattices constructed from C_4 rotational symmetric sublattices with a Moiré angle 2ϑ = arctan(3/4) and a TAM quantum number l =7 can be considered a combination of skyrmions with a topological skyrmion number $n_{sk} = \pm 1$, as shown in **FIG. S**9(a-b). Similarly, for Moiré lattices derived from C_3 rotational symmetric sublattices with a Moiré angle 2ϑ = arccos(1/7) and $l = 8$, the unit cell can also be regarded as a combination of skyrmions with a topological skyrmion number $n_{sk} = \pm 1$, as depicted in **FIG. S**9(c-d). The corresponding experimental results are summarized in **FIG. S**14 to **FIG. S**15.

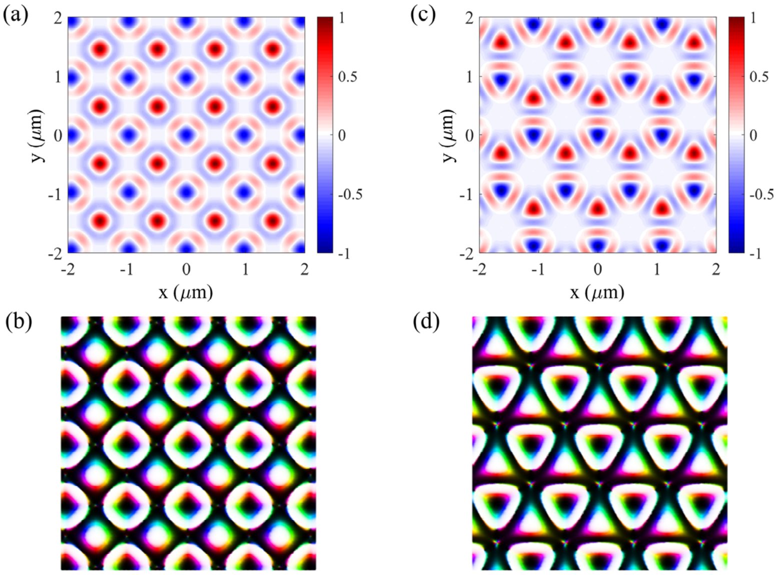

FIG. S9. Moiré lattices featuring unit cell composed of skyrmions with topological skyrmion number $n_{sk} = \pm 1$. (a) The distribution of S_z and (b) the corresponding topological spin texture for the Moiré lattices constructed from C_4 rotational symmetric sublattices, characterized by a Moiré angle 2ϑ = arctan(3/4) and a TAM quantum number l =7. (c) The distribution of S_z and (d) the associated topological spin texture for the Moiré lattices formed by C_3 rotational symmetric sublattices, with a Moiré angle 2ϑ = arccos(1/7) and $l = 8$.

Arbitrarily tunable Meron geometric clusters

Skyrmion cluster states refer to stable, high-degree multi-skyrmion configurations in which an arbitrary number of antiskyrmions are contained within a larger skyrmion [S7-S9]. These states have been widely observed in experiments within the realm of condensed matter physics. In this context, we demonstrate that meron geometric clusters can also be formed through Moiré lattice, with tunability based on the quantum number l of TAM. For example, in Moiré lattices constructed from C_4 rotational symmetric sublattices, with a Moiré angle 2ϑ =

arctan(8/15) and TAM quantum number l = 2, 4, 8, and 10, meron cluster-like textures emerge. Notably, the topological skyrmion number and the orientations of the photonic meron geometric clusters can be finely tuned, as illustrated in **FIG. S**10. The corresponding experimental results are summarized in **FIG. S**16 to **FIG. S**19.

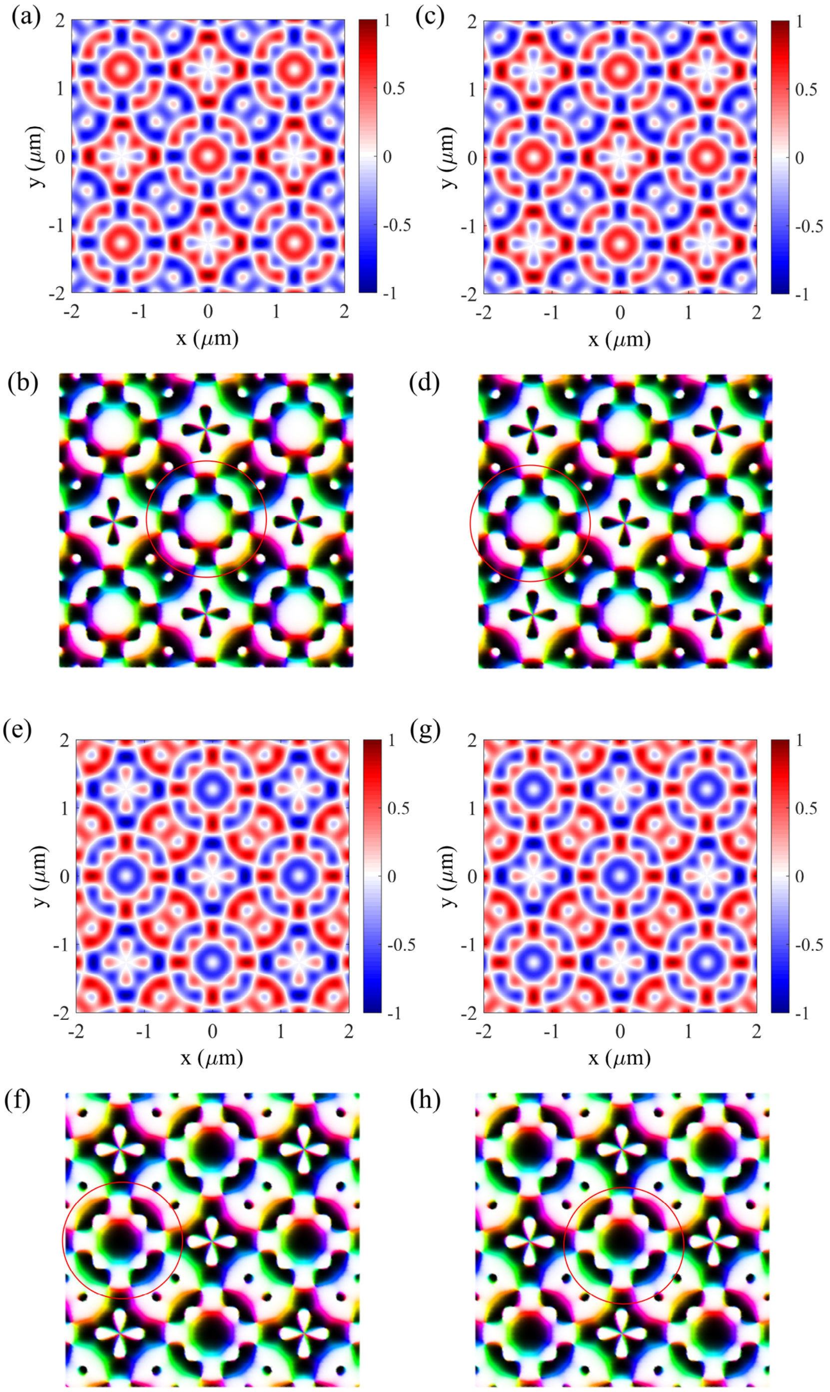

FIG. S10. Meron-geometric cluster topologies in photonic Moiré lattices. (a) The distribution of S_z and (b) the topological spin texture for the Moiré lattices constructed from C_4 rotational symmetric sublattices with a Moiré angle 2ϑ = arctan(8/15) and a quantum number of TAM l = 2. (c) and (d) show the same distribution for S_z and topological spin texture as (a) and (b), respectively, but for l = 4; (e) and (f) present similar data for l = 8; while (g) and (h) illustrate the same for l = 10. The meron-geometric cluster states can be clearly identified within the red circles.

Multiple Fractal patterns

To illustrate the fractal properties, we consider the Moiré lattices constructed by the 3-fold symmetric sublattices.

The SAM can be expressed as

$$S_z = \frac{\varepsilon |A|^2 e^{-2k_z z}}{2\omega} \left\{ \begin{array}{l} +\frac{\sqrt{3}}{2}\sin\left[+\sqrt{3}\beta\left[x\sin[\vartheta] - y\cos[\vartheta] \right] - l\frac{4\pi}{3} \right] \\ -\sqrt{3}\sin\left[+\frac{\sqrt{3}}{2}\beta\left[x\sin[\vartheta] - y\cos[\vartheta] \right] - l\frac{2\pi}{3} \right]\cos\left[+\frac{3}{2}\beta\left[x\cos[\vartheta] + y\sin[\vartheta] \right] \right] \end{array} \right\}. \quad \text{(S28)}$$

For the Moiré lattices constructed by the 3-fold symmetric sublattices, we analyze the case where the Moiré angle is given by $2\vartheta = \arccos(-1/26)$ and the incident quantum number of the TAM is $l = 10$. The z-component of the SAM density can be found in **FIG. S**11(a), and one can find that there will be four distinct sets of wavenumbers in the Fourier space, as shown in **FIG. S**11(b). This indicates the complex periodic structure and the multifaceted nature of the topological spin configurations in the system.

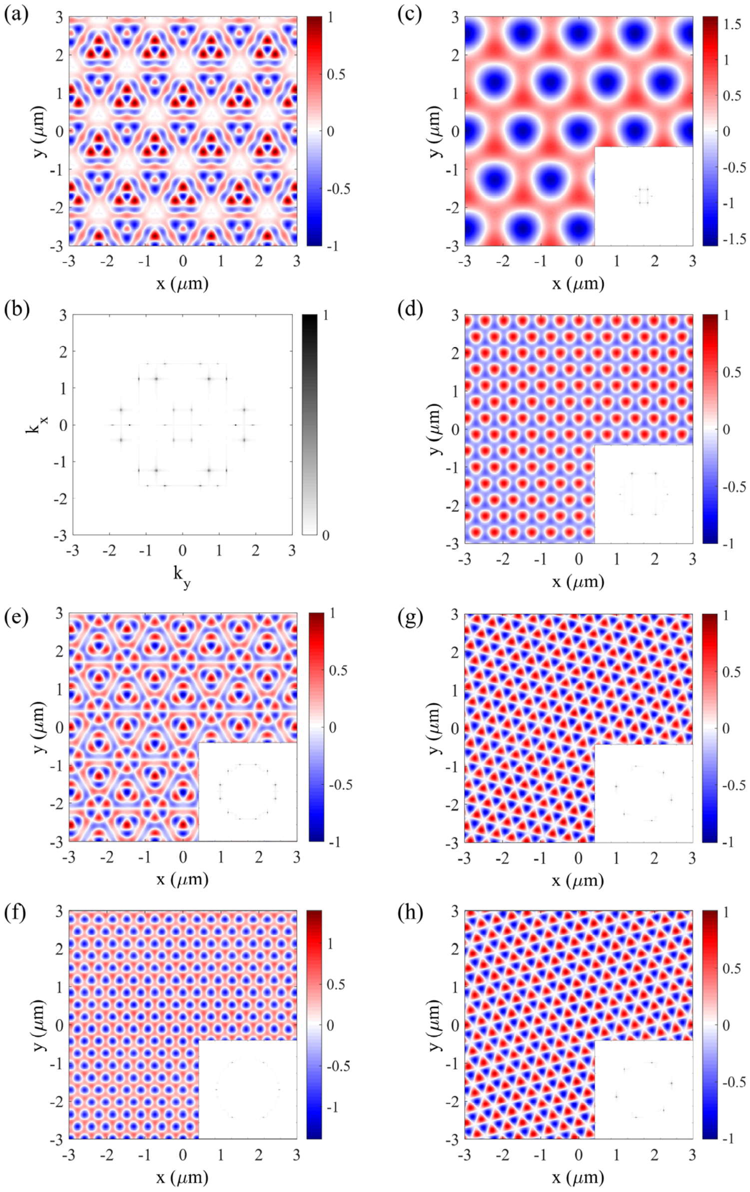

FIG. S11. Fractal patterns in photonic Moiré lattices. (a) The S_z component and the corresponding (b) wavenumber distribution in Fourier space of the Moiré lattice formed from C_3 rotational symmetric sublattices when $l = 10$ and the Moiré angle $2\vartheta = \arccos(-1/26)$. The extracted fractal lattices in the Moiré lattice for the (c) central, (d) second, (e) third and (f) fourth sets of wavenumbers. Therein, the extracted fractal lattice corresponding to the third set of wavenumbers can be divided into two sets of sublattices (g) and (h) owing to the Moiré property of the lattice. The inset images show the wavenumbers in Fourier space corresponding to the extracted fractal lattices, highlighting their spatial arrangement and properties.

By extracting the separated sets of wavenumbers and carrying out the inverse Fourier transformation, three distinct sets of C_3 rotational symmetric lattices are obtained, represented in **FIG. S**11(c), **FIG. S**11(d) and **FIG. S**11(f), respectively. *The left one set shown in **FIG. S**11(e) contains a pair of sublattices resulting from the Moiré property of the lattice*. This emphasizes the complex interactions within the lattice structure. Careful selection of inclination angles allows for the extraction of two distinct C_3 rotational symmetric sublattices, depicted in **FIG. S**11(g) and **FIG. S**11(h), respectively. It can be observed that the orientations of both sublattices are confirmed to be inclined, supporting the earlier analysis regarding their formation. Moreover, all lattices displayed in **FIG. S**11(c-h) exhibit C_3 rotational symmetry, further illustrating the fractal properties inherent in the Moiré lattices. Remarkably, the Moiré lattices are subject to diffraction limits. The maximal wavenumber cannot exceed $2k$, where k is the wavenumber in free space. This implies that the scale of optical fractal lattices cannot become indefinitely small. This characteristic presents a significant distinction between optical fractal phenomena and natural fractals. The corresponding experimental results confirming these observations are summarized in **FIG. S**20.

Extreme Slow-light control

Interestingly, despite the absence of localization in photonic Moiré topological spin lattices, these lattices exhibit a significant property of slow light. It is known that the group velocity of SPP plane wave is defined as $v_{\text{gp}} = kc/\beta < c$ [S10]. For photonic Moiré topological spin lattices, the local group velocity can be calculated as the ratio of the Poynting vector (which is proportional to kinetic Poynting momentum) to energy density. Notably, this local group velocity can be significantly lower than that of the SPP plane wave, $v_{\text{gp}} = kc/\beta$. For a Moiré lattice constructed by the C_4 rotational symmetric sublattices with a Moiré angle $2\vartheta = \arctan(5/12)$ and quantum number of angular momentum $l = 16$, the maximal local group velocity is observed to be below one-tenth of the group velocity of the SPP plane wave $\underline{v}_{\text{gp}}$ in air half-space, as shown in **FIG. S**12(e) and **FIG. S**12(f). The reduced group velocity is attributed to the formation of local vortex-antivortex flux within the Moiré lattice (**FIG. S**12(d)). This off-axis vortex-antivortex flux is closely linked to optical super-oscillation [S11, S12], allowing for the creation of deep-subwavelength fine spin structures within confined optical fields [S13]. The unique properties of these spin structures hold potential for applications in picometer metrology [S14-S16], indicating a promising area for future research and technological development. The corresponding experimental results confirming these phenomena are summarized in **FIG. S**21.

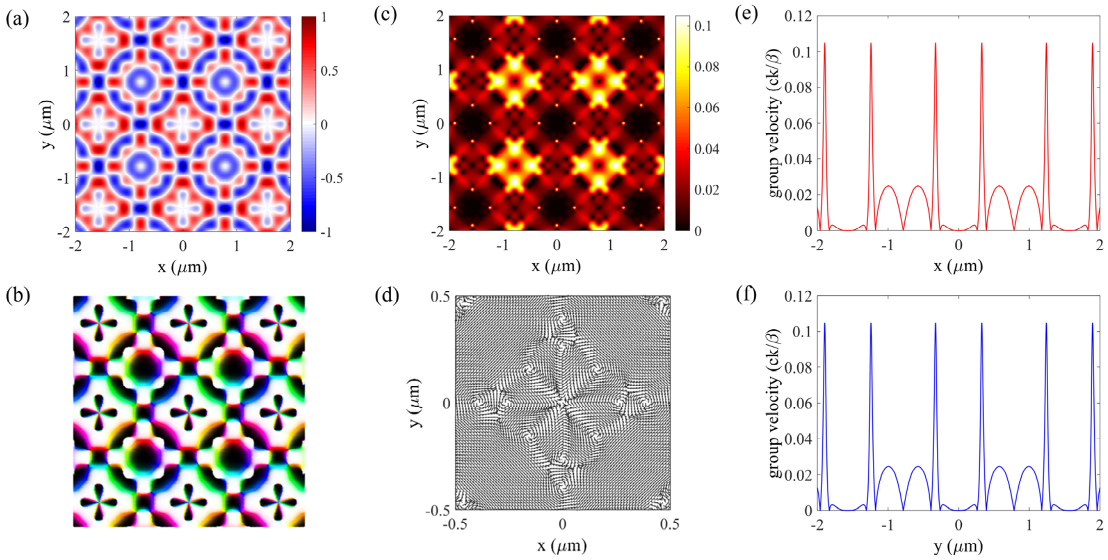

FIG. S12. Slow light effect in Moiré spin lattice. (a) The S_z component and (b) the topological spin texture of the Moiré lattice formed by C_4 rotational symmetric sublattices with $l = 16$ and a Moiré angle $2\vartheta = \arctan(5/12)$ are illustrated. (c) The local group velocity, calculated as the ratio of kinetic Poynting momentum to energy density, is observed to be approximately one-tenth of the group velocity of SPP in air half space. The reduced group velocity is attributed to the formation of (d) local vortex-antivortex momentum flux, which is intricately linked to optical super-oscillation. The 1D contours of group velocities in the x- and y-directions are presented in (e) and (f), respectively, providing insight into the anisotropic nature of the group velocity within the lattice.

V. Experimental characterization of photonic Moiré spin superlattices

The experimental setup for the demonstration of the photonic Moiré lattices is shown in **FIG. S**13(a). The experiment was performed on the example of surface plasmon polaritons (SPPs), which are excited on a surface of a thin gold film (50nm) with an oil-immersion objective lens (Olympus, 100×, NA=1.49). A linearly polarized beam with wavelength of 632.8nm from He-Ne laser was used as an excitation source. The incident beam with desired linear polarization by passing through a linear polarizer (LP) and a half-wave plate (HWP) was modulated by a spatial light modulator (SLM) with the phase expressed by

$$\psi=\arg\left[\sum_{n=1}^{N} e^{ik_t(x\cos(\theta_n+\vartheta)+y\sin(\theta_n+\vartheta))}e^{il(\theta_n+\vartheta)}+\sum_{n=1}^{N} e^{ik_t(x\cos(\theta_n-\vartheta)+y\sin(\theta_n-\vartheta))}e^{il(\theta_n-\vartheta)}\right] \tag{S29}$$

to generate the desired pair of plane wave. The parameter k_t should be chosen carefully to match the size of beam with the pupil of objective lens. The parameter l can be tuned to generate the vortex phase carrying desired quantum number. Then, the beams pass through a HWP and 1-order vortex-wave plate (VWP) to generate the radially polarized light, which is tightly focused by an oil immersion objective lens (Olympus, NA=1.49, 100×) to excite the SPP plane waves on the gold film.

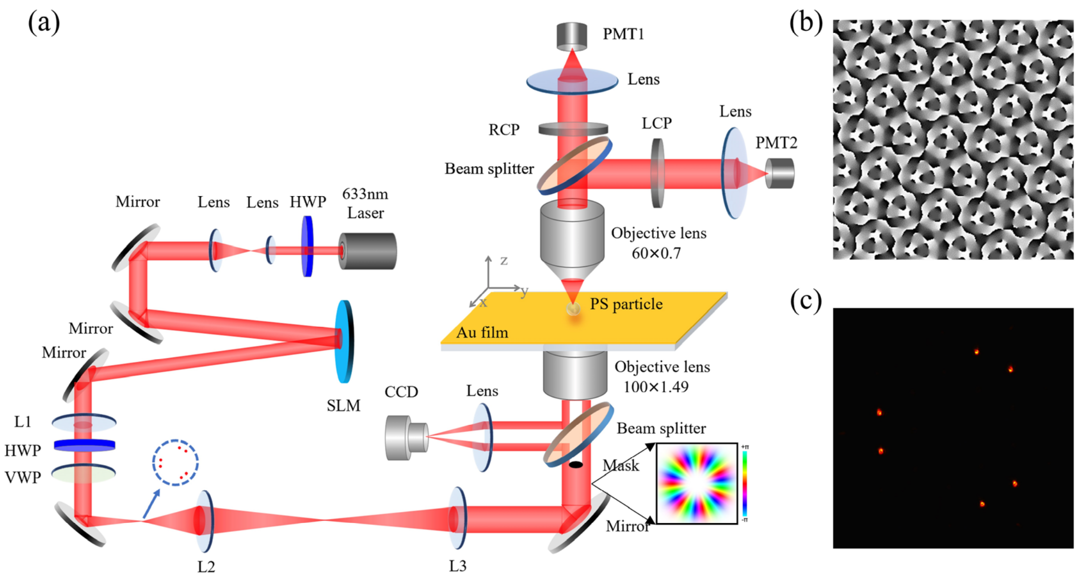

FIG. S13. (a) Experimental setup. (b) The phase distribution in the SLM to generate the photonic Moiré lattice consisting of a pair of the C_3 rotational symmetric sublattices with the Moiré angle $2\vartheta = \arccos(-1/26)$; (c) The image captured by CCD at the back focal plane (BFP) of oil-immersed objective lens.

The surface electromagnetic field was measured by an in-house near-field scanning optical microscopic system (NSOM) with a PS nanoparticle probe with diameter 300nm sitting on a gold film. The position of the PS particle can be precisely controlled by a piezo-stage (Physik Instrumente, P-545). The near-field signal that is scattered by the PS particle to an objective lens (Olympus, NA = 0.7, 60×) acting as a low-pass filter was split and then analyzed using a combination of a QWP and a LP to extract the individual circular polarization component (I_{LCP}: left-handed circularly polarized component and I_{RCP}: right-handed circularly polarized component) of the scattering signal. Through the dipole theory [S17, S18], the horizontal components of electric field can be reconstructed. These components were then directed to two photomultiplier tubes (PMTs) to measure the intensity information of the two signals. Then, it enables characterization of the out-of-plane SAM component (i.e., along the optical axis) of the focused beams by the relation [S19]:

$$S_z = \frac{\varepsilon}{4\omega}\frac{\beta^2}{k_z^2}\left(I_{\mathrm{RCP}} - I_{\mathrm{LCP}}\right) \propto I_{\mathrm{RCP}} - I_{\mathrm{LCP}} \quad . \tag{S30}$$

We take the Moiré lattices consisting of a pair of the C_3 rotational symmetric sublattices with Moiré angle $2\vartheta = \arccos(-1/26)$ for example. The linearly polarized beam after a beam expander illuminates on the SLM with the incident angle smaller than 10° will carry an additional phase ψ, as shown in **FIG.** S13(b). This beam will form 6 focuses at focal plane after Fourier transform achieved by a lens with focal length f = 500mm. These 6 focuses can be decomposed into 2 groups, in which one group can be regarded as a rotation of another group with Moiré angle $2\vartheta = \arccos(-1/26)$ as shown in **FIG.** S13(c). The measured circularly polarized components, the reconstructed S_z and spin textures and the corresponding theoretical results can be found in from **FIG.** S14 to **FIG.** S21.

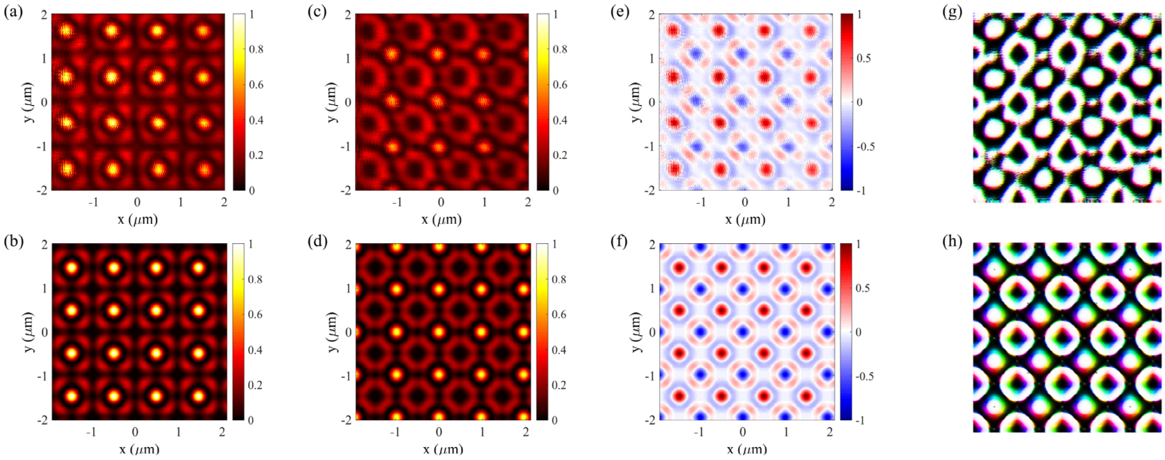

FIG. S14. Experimental observations for the (a) I_{RCP}, (c) I_{LCP}, (e) S_z component and (g) reconstructed topological texture formed by C_4 rotational symmetric sublattices. Here, the Moiré angle $2\vartheta = \arctan(3/4)$ and the quantum number of incident TAM $l = 7$. Its unit cell be considered as the combination of skyrmions with skyrmion number $n_{sk} = \pm1$. The corresponding theoretical results can be found in (b), (d), (f) and (g).

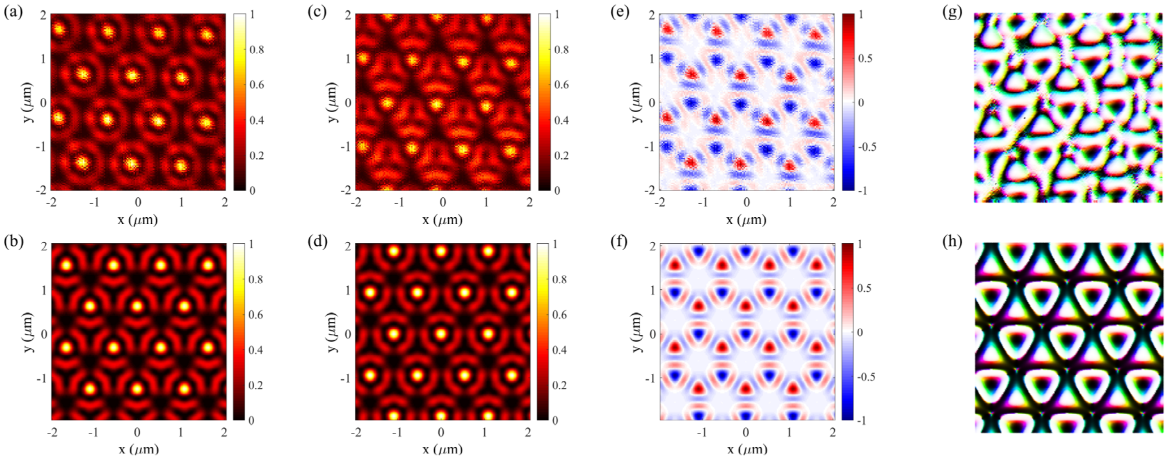

FIG. S15. Experimental observations for the (a) I_{RCP}, (c) I_{LCP}, (e) S_z component and (g) reconstructed topological texture formed by C_4 rotational symmetric sublattices. Here, the Moiré angle $2\vartheta = \arccos(1/7)$ and the quantum number of incident TAM $l = 8$. Its unit cell be considered as the combination of skyrmions with skyrmion number $n_{sk} = \pm1$. The corresponding theoretical results can be found in (b), (d), (f) and (g).

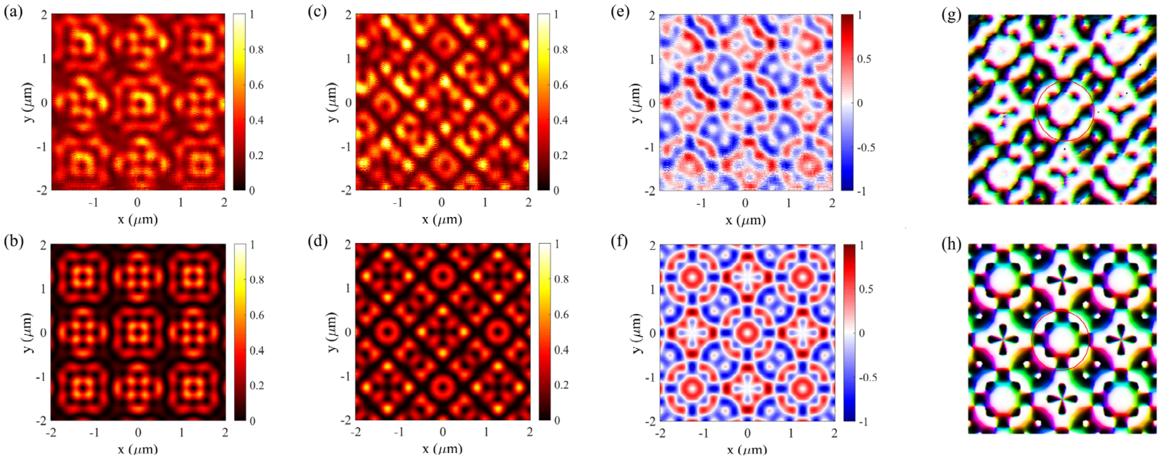

FIG. S16. Experimental observations for the (a) I_{RCP}, (c) I_{LCP}, (e) S_z component and (g) reconstructed topological texture formed by C_4 rotational symmetric sublattices. Here, the Moiré angle $2\vartheta = \arctan(8/15)$ and the quantum number of incident TAM $l = 2$. The corresponding theoretical results can be found in (b), (d), (f) and (h) represents the spin textures. The meron geometric cluster -like spin textures can be found in the red circles in (g), (h).

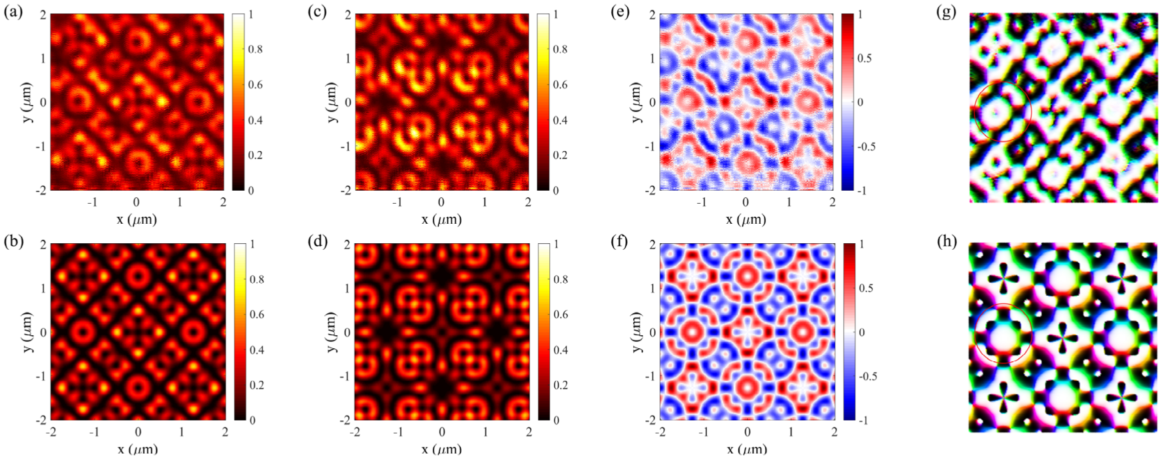

FIG. S17. Experimental observations for the (a) I_{RCP}, (c) I_{LCP}, (e) S_z component and (g) reconstructed topological texture formed by C_4 rotational symmetric sublattices. Here, the Moiré angle $2\vartheta = \arctan(8/15)$ and the quantum number of incident TAM $l = 4$. The corresponding theoretical results can be found in (b), (d), (f) and (h) represents the spin textures. The meron geometric cluster -like spin textures can be found in the red circles in (g), (h).

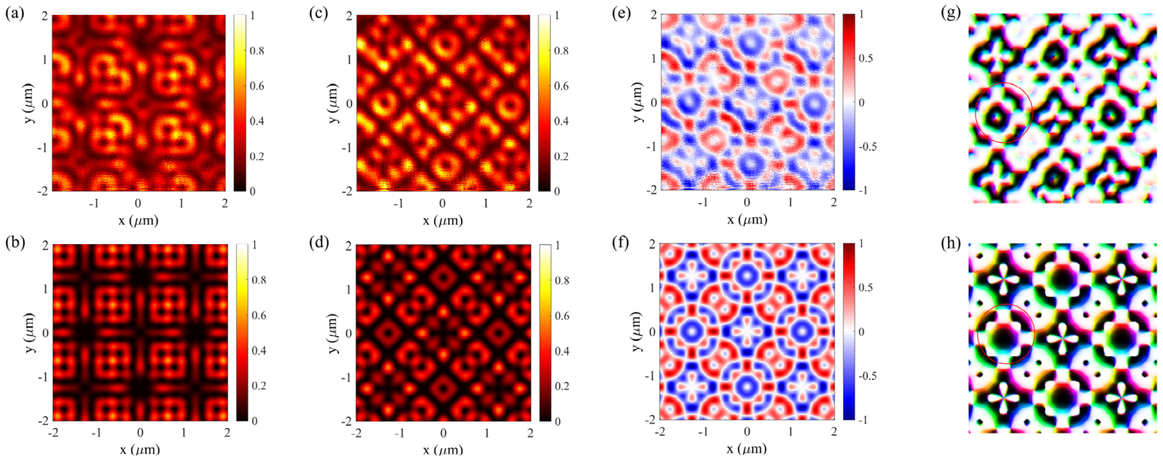

FIG. S18. Experimental observations for the (a) I_{RCP}, (c) I_{LCP}, (e) S_z component and (g) reconstructed topological texture formed by C_4 rotational symmetric sublattices. Here, the Moiré angle $2\vartheta = \arctan(8/15)$ and the quantum number of incident TAM $l = 8$. The corresponding theoretical results can be found in (b), (d), (f) and (h) represents the spin textures. The meron geometric cluster -like spin textures can be found in the red circles in (g), (h).

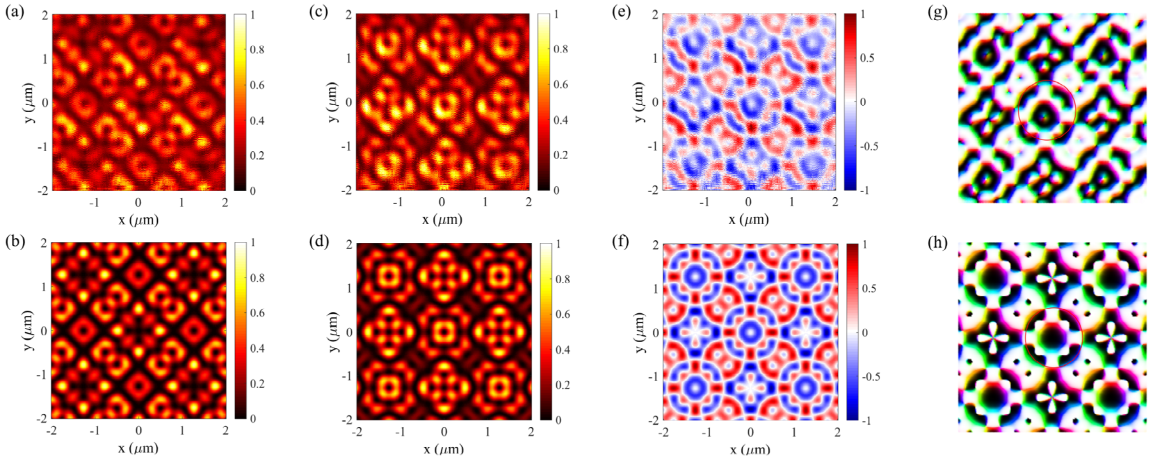

FIG. S19. Experimental observations for the (a) I_{RCP}, (c) I_{LCP}, (e) S_z component and (g) reconstructed topological texture formed by C_4 rotational symmetric sublattices. Here, the Moiré angle $2\vartheta = \arctan(8/15)$ and the quantum number of incident TAM $l = 10$. The corresponding theoretical results can be found in (b), (d), (f) and (h) represents the spin textures. The meron geometric cluster -like spin textures can be found in the red circles in (g), (h).

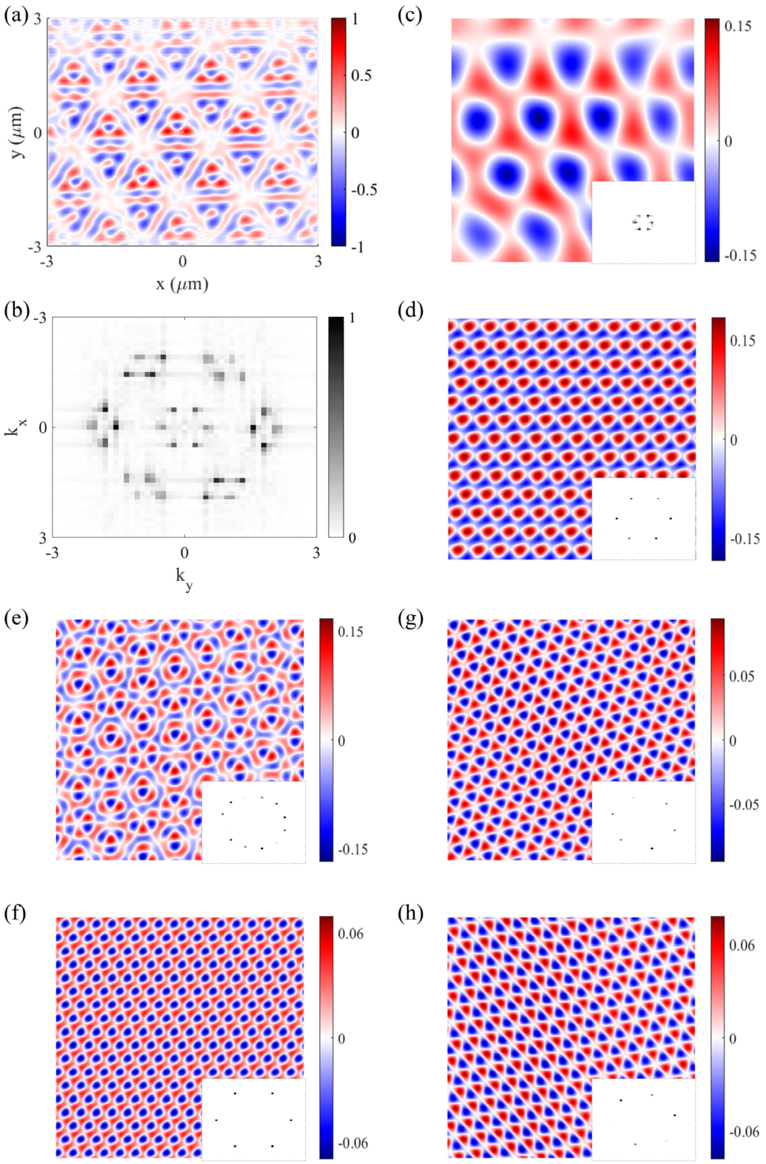

FIG. S20. Fractals in photonic Moiré lattices. The experimental (a) S_z component and the corresponding (b) wavenumber in Fourier space of Moiré lattice formed by the C_3 rotational symmetric sublattice when $l = 10$ and the Moiré angle $2\vartheta = \arccos(-1/26)$. The extracted fractal lattices in the Moiré lattice for the (c) central, (d) second, (e) third and (f) fourth sets of wavenumbers. Therein, the extracted fractal lattice corresponding to the third set of wavenumbers can be divided into two sets of sublattices (g) and (h) owing to the Moiré property of the lattice. The inset images show the wavenumbers in Fourier space. The theoretical results can be found in **FIG. S**11.

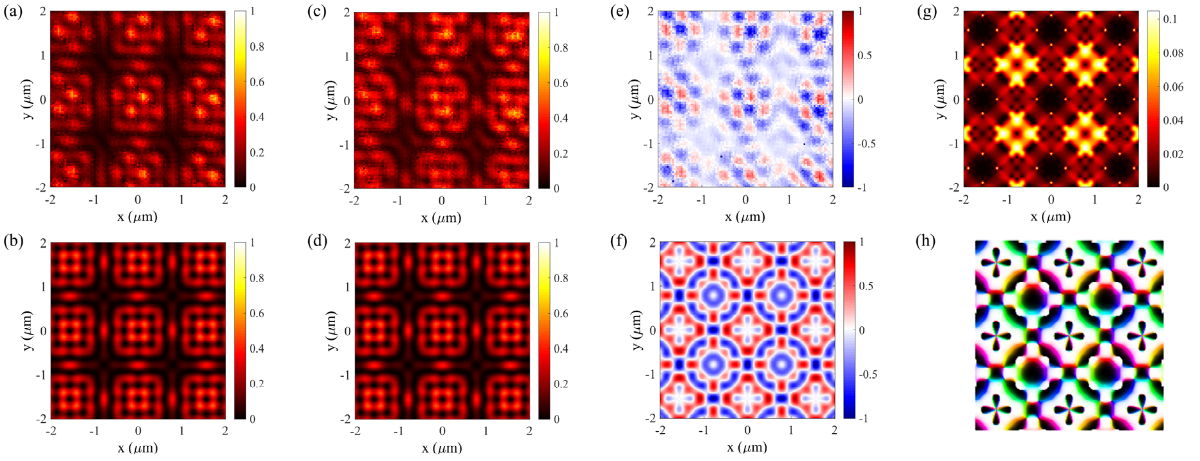

FIG. S21. The experimental (a) I_{RCP}, (c) I_{LCP} and (e) S_z component distributions for the Moiré spin lattice formed by the C_4 rotational symmetric sublattices. Here, the Moiré angle is $2\vartheta = \arctan(5/12)$ and the quantum number of incident TAM is $l = 16$. The corresponding theoretical results can be found in (b), (d) and (f). The slow light effect can be found in (g), where the group velocity is normalized by the group velocity of SPP plane wave (kc/β) in the air half-space.The maximal local group velocity for the Moiré lattice is about one-tenth of the velocity of light in vacuum. The theoretical spin texture is shown in (h).

REFERENCES

[S1] A. V. Zayats, I. I. Smolyaninov, and A. A. Maradudin, Nano-optics of surface plasmon polaritons, Phys. Rep. **408**(3–4), 131–314 (2005).

[S2] Q. Zhang, A. Yang, Z. Xie, P. Shi, L. Du, and X. Yuan, Periodic dynamics of optical skyrmion lattices driven by symmetry, Appl. Phys. Rev. **11**, 011409 (2024).

[S3] X. Lei, A. Yang, P. Shi, Z. Xie, L. Du, A. V. Zayats, and X. Yuan, Photonic spin lattices: symmetry constraints for skyrmion and meron topologies, Phys. Rev. Lett. **127**, 237403 (2021).

[S4] P. Shi, L. Du, C. Li, A. V. Zayats, and X. Yuan, Transverse spin dynamics in structured electromagnetic guided waves, Proc. Natl. Acad. Sci. U.S.A. **118**, e2018816118 (2021).

[S5] Naoto Nagaosa and Yoshinori Tokura, Topological properties and dynamics of magnetic skyrmions, Nat. Nanotechnology **8**, 899–911, (2013).

[S6] P. Wang, Y. Zheng, X. Chen, C. Huang, Y. V. Kartashov, L. Torner, V. V. Konotop, and F. Ye, Localization and delocalization of light in photonic Moiré lattices, Nature **577**, 42–46 (2020).

[S7] J. Müller, J. Rajeswari, P. Huang, Y. Murooka, H. M. Rønnow, F. Carbone, and A. Rosch, Magnetic Skyrmions and Skyrmion Clusters in the Helical Phase of Cu_2OSeO_3, Phys. Rev. Lett. **119**, 137201 (2017).

[S8] X. Zhao, C. Jin, C. Wang, H. Du, J. Zang, M. Tian, R. Che, and Y. Zhang, Direct imaging of magnetic field-driven transitions of skyrmion cluster states in FeGe nanodisks, Proc. Natl. Acad. Sci. U.S.A. **113**, 4918-4923 (2016).

[S9] D. Foster, C. Kind, P. J. Ackerman, Jung-Shen B. Tai, M. R. Dennis, and Ivan I. Smalyukh, Two-dimensional skyrmion bags in liquid crystals and ferromagnets, Nat. Phys. **15**, 655–659 (2019).

[S10] Konstantin Y. Bliokh and Franco Nori, Transverse spin of a surface polariton, Phys. Rev. A **85**, 061801(R) (2012).

[S11] N. I. Zheludev and G. Yuan, Optical superoscillation technologies beyond the diffraction limit, Nat. Rev. Phys. **4**, 16–32 (2022).

[S12] G. Yuan, E.T.F. Rogers, N. I. Zheludev, "Plasmonics" in free space: observation of giant wavevectors, vortices, and energy backflow in superoscillatory optical fields, Light Sci. Appl. **8**, 2 (2019).

[S13] L. Du, A. Yang, A.V. Zayats, and X. Yuan, Deep-subwavelength features of photonic skyrmions in a confined electromagnetic field with orbital angular momentum. Nat. Phys. **15**, 650–654 (2019).

[S14] Tongjun Liu, Cheng-Hung Chi, Jun-Yu Ou, Jie Xu, Eng Aik Chan, Kevin F. MacDonald, and Nikolay I. Zheludev, Picophotonic localization metrology beyond thermal fluctuations. Nat. Mater. 22, 844–847 (2023).

[S15] Nikolay I. Zheludev and Kevin F. MacDonald, The Birth of Picophotonics, Optics & Photonics News **34**, 36-41 (2023).

[S16] Aiping Yang, Xinrui Lei, Peng Shi, Fanfei Meng, Min Lin, Luping Du, Xiaocong Yuan, Spin-Manipulated Photonic Skyrmion-Pair for

Pico-Metric Displacement Sensing, Adv. Sci. 10(12), 2205249 (2023).

[S17] Aiping Yang, Jiashuo Chen, Xusheng Chen, Fanfei Meng, Luping Du, Xiaocong Yuan, Three orthogonal polarization distribution mapping of the tightly focused fields with a dual-mode waveguide probe, Laser & Photonics Reviews **17**(12), 2300032 (2023).

[S18] P. Shi, A. Yang, F. Meng, J. Chen, Y. Zhang, Z. Xie, L. Du, and X. Yuan, Optical near-field measurement for spin-orbit interaction of light, Progress in Quantum Electronics **78**, 100341 (2021).

[S19] C. Li, P. Shi, L. Du and X. Yuan, Mapping the near-field spin angular momenta in the structured surface plasmon polariton field, Nanoscale **12**, 13674 (2020).